Materials & Design 266 (2026) 116126

Contents lists available at ScienceDirect

Materials & Design

journal homepage: www.elsevier.com/locate/matdes

Additive manufacturing of polymer-derived SiOC(Fe) ceramic composites as a catalyst support exhibiting magnetic heating capability

Milan Vukšić [a,*], Thomas Konegger [b], Martin Schwentenwein [c], Sašo Gyergyek [d], Anja Sedminek [d], Sandra Drev [e], Marijan Nečemer [f], Andraž Kocjan [a], Aljaž Iveković [a,*]

[a] Department for Nanostructured Materials, Jožef Stefan Institute, Jamova cesta 39, 1000 Ljubljana, Slovenia
[b] Institute of Chemical Technologies and Analytics, TU Wien, Getreidemarkt 9, 1060 Vienna, Austria
[c] Lithoz GmbH, Mollardgasse 85a/2/64-69, 1060 Vienna, Austria
[d] Department for Materials Synthesis, Jožef Stefan Institute, Jamova cesta 39, 1000 Ljubljana, Slovenia
[e] Center for Electron Microscopy and Microanalysis (CEMM), Jožef Stefan Institute, Jamova cesta 39, 1000 Ljubljana, Slovenia
[f] Department for Low and Medium Energy Physics, Jožef Stefan Institute, Jamova cesta 39, 1000 Ljubljana, Slovenia

ARTICLE INFO

Keywords:
Vat photopolymerization
Polymer-derived ceramics
Magnetic nanoparticles
Ceramic nanocomposite
Induction/magnetic heating

ABSTRACT

Additive manufacturing (AM) of advanced functional ceramics using preceramic polymers (PCPs) is gaining attention due to its processability and tailorable properties. A photosensitive resin with iron-modified polysiloxanes was developed for vat photopolymerization (VPP) to create porous SiOC(Fe) catalytic supports with magnetic heating capability. Ferric acetylacetonate and ferrocene were examined as iron precursors, leading to the formation of Fe-based magnetic particles (α-Fe, Fe_3C, Fe_xSi_y) within the silicon oxycarbide (SiOC) ceramic matrix after pyrolysis at 800 to 1500 °C. Depending on the Fe-based precursor used and the applied pyrolysis temperature, the obtained monoliths exhibited magnetic nanoparticle (MNP) contents ranging from 0.9 to 7.9 wt %, with particle sizes from 17 to 96 nm. The monolithic catalyst supports fabricated from ferric acetylacetonate modified PCP-based resin formulations, pyrolyzed at 900 °C, exhibited the highest specific absorption rate and resulted in magnetic heating up to 200 °C at an applied external magnetic field of 60 $kA{\cdot}m^{-1}$. While catalyst supports fabricated from ferrocene modified PCP-based resin formulations had lower heating capabilities, they offered better printability and higher ceramic yield. In situ formed MNPs impart magnetic properties advantageous for catalyst support heating, highlighting AM's design flexibility and PCPs' role in creating tailored, lightweight structures with controlled porosity.

1. Introduction

To reduce the carbon footprint associated with the production of fuel and commodity chemicals, there is an increasing need for the electrification of the chemical industry [1]. Conventional catalytic reactors require time- and energy-demanding heating, often associated with burning of fossil fuels, resulting in significant amounts of greenhouse emissions. Alternatively, magnetic or induction heating of magnetic nanoparticles embedded in a catalyst framework offers rapid, more homogenous and on-demand heating [2], thus eliminating the drawbacks of conventional passive catalytic reactors.

When magnetic nanoparticles (MNPs) (<100 nm) embedded in the catalytic support are exposed to a radiofrequency alternating magnetic field, heat is generated within them, leading to rapid and selective heating of the catalyst support. Heating is achieved through different heating mechanisms that can vary depending on the physical and magnetic properties, as well as the size of the material [2]. In the case of ferromagnetic materials, the heat is generated by alternating magnetization and hysteresis losses due to friction between the molecules when the material is continuously magnetized in various directions [3].

Shaping of catalytic supports typically involves the extrusion of relatively simple shapes with unidirectionally aligned channels (e.g. honeycombs). Although such structures are easy to fabricate, they have certain drawbacks, such as limited surface area and conversion efficiency [4]. Decorating extruded catalyst frameworks with MNPs represents an additional synthesis and calcination step, where homogeneous deposition and adhesion of MNPs can be challenging [5].

Additive manufacturing (AM), on the other hand, facilitates shaping

* Corresponding authors.
E-mail addresses: milan.vuksic@ijs.si (M. Vukšić), aljaz.ivekovic@ijs.si (A. Iveković).

https://doi.org/10.1016/j.matdes.2026.116126
Received 24 February 2026; Received in revised form 3 April 2026; Accepted 26 April 2026
Available online 27 April 2026

of catalytic frameworks with an engineered, unprecedented structural and geometrical freedom to balance high active surface area and low pressure drop [6]. Among the numerous AM techniques [7], Vat photopolymerization (VPP) techniques, particularly via DLP (Digital Light Processing), are considered as state-of-the-art for manufacturing ceramic components. The process relies on the selective curing of a suspension consisting of a photosensitive resin highly filled with ceramic particles (>40 vol%) by light [8]. However, the introduction of nano-sized powders such as MNPs into the photopolymerizable resin is challenging, as they greatly affect the rheological behavior, while the dark color of MNPs results in high light absorption and light scattering, both resulting in limited printability of photosensitive resins similar to ceramic suspensions [9].

A promising alternative is to employ VPP for the crosslinking of preceramic polymers (PCPs) for the AM of complex structures, since PCPs are highly soluble in organic solvents and suitable for photosensitive resin preparation [10]. A subsequent pyrolysis treatment (400–1400 °C), the so-called ceramization process, transforms the preceramic polymer from an organic to an inorganic state, and it has a crucial effect on the composition, ceramic yield, structure, and properties of the final ceramic or ceramic composite material. Additional functional properties of polymer derived ceramics (PDC) can be achieved by blending the polymer with inorganic metal compounds (e.g. metallic nanoparticles) [11] or by modifying the polymer chain by introducing organometallic compounds [12]. The latter approach enables the modification of polymers at an atomic scale, resulting in a more homogeneous distribution of *in situ* formed nanoparticles within the PDC matrix. Employing Fe-based precursors for the modification of PCPs was already successfully performed to form PDCs composites exhibiting electromagnetic properties using traditional methods such as pressing or molding. For this purpose, PCPs were typically modified by ferric acetylacetonate, which resulted in the formation of α-Fe and various iron silicide nanoparticles (Fe_xSi_y) depending on the pyrolysis temperature [13,14]. Alternatively, Yu et al. [15] mixed allylhydridopolycarbosilane (AHPCS) with different contents of vinyl ferrocene (VF) to synthetize hyperbranched polyferrocene carbosilane, which was subsequently pyrolyzed in the range from 900 °C to 1300 °C. The samples exhibited magnetic properties due to *in situ* formation of α-Fe during pyrolysis in the temperature range from 900 °C to 1300 °C. The existence of elemental iron at higher temperatures was justified by the lack of interdiffusion of the turbostratic carbon layers located at the segregated α-Fe crystal boundaries. The above studies indicate that by adjusting the pyrolysis temperature and heating rate, the size and phase composition of precipitated iron particles can be fine-tuned to regulate the magnetic properties of the ceramic composite material.

Although Fe-modified PCPs have been utilized to produce PDC matrix composites, their integration into VPP processes has been limited. The majority of the reported research focused on the preparation of bulk ceramics, where the addition of Fe-based organometallics was used to catalyze the *in situ* generation of nanofibers or carbon nanotubes within the PDC matrix to improve the mechanical and microwave-absorbing properties [16]. Lin et al. [17] developed DLP-suitable photosensitive resin blends of acrylates, organic solvents, polysiloxane powder as silicone source, and vinyl-ferrocene as filler. Samples pyrolyzed up to 1000 °C resulted in the formation of carbon nanowires, accompanied by an Fe_3C phase. Feng et al. [18] prepared resins by simple blending of polysilazane powder with 1.5 wt% of ferrocene with respect to the amount of polysilazane, and a commercially available photosensitive polymer. During pyrolysis, ferrocene catalyzed the *in situ* formation of a large amount of turbostratic carbon, graphite, and nanosized SiC, which enabled electromagnetic wave absorption performance of SiCN(Fe) ceramic. The iron content was not reported due to the low sensitivity of the analytical technique employed.

The objective of this work is to systematically evaluate PCP-based photopolymerizable resin formulations containing different Fe-based precursors, namely ferric acetylacetonate and ferrocene, as feedstocks in the DLP workflow for the fabrication of porous catalyst supports. The subsequent pyrolysis of the formed resin systems results in a polymer-to-ceramic conversion, yielding mesoporous SiOC with homogeneously distributed *in situ* formed Fe-based magnetic nanoparticles. This "*functionalization*" of the 3D-printed structures introduces magnetic heating capability. The goal of this work is thus to study the effect of the resin composition (i.e., the choice of iron precursor), and pyrolysis conditions on the size and phase composition of the *in situ* formed iron nanoparticles, affecting the final magnetic properties. The magnetic heating capability of the obtained SiOC(Fe) monoliths is investigated for the potential application as catalyst supports in electrified catalytic processes.

2. Experimental

2.1. Materials

Two types of Fe-based precursors, ferric (III) acetylacetonate ($Fe(acac)_3$, 98 %, Alfa Aesar, USA) and ferrocene ($Fe(cp)_2$, 98 %, Thermo Scientific Chemicals, USA), were used to modify a commercially available preceramic polymer, methyl-silsesquioxane (PSO; SilresMK, Wacker, Germany). The solvents in which modification occurred were anhydrous o-xylene (>95 %, VWR Chemicals, USA), or toluene (>95 %, VWR Chemicals, USA) in the case of ferrocene precursor. For the preparation of the photosensitive resin, tri(propyleneglycol)-methyl ether (TPM, Formlabs, USA) was used as solvent, trimethylolpropane-trimethacrylate (TMPTMA, 85 %, Sigma–Aldrich, USA) was used as photosensitive acrylate, and tetraethylorthosilicate (TEOS, 98 %, Sigma–Aldrich, USA) was used as solubilizing agent. Two different radical scavengers, commercially available as Genorad 16 and Genorad 21 (Rahn AG, Switzerland), were added to increase the stability of the Fe-modified resins against premature gelation. A proprietary type I photoinitiator (Lithoz GmbH, Austria) was employed as photoinitiator.

2.2. Preparation of photosensitive resins for the VPP process

The photosensitive resin was prepared according to the approach reported by Essmeister at al. [19]. This approach was purposely selected due to reported vat photopolymerization-induced phase separation for the generation of hierarchically porous ceramics. Minor variations were implemented to enable the successful printing of the resulting photosensitive resin. The modification of the PSO by ferric acetylacetonate was conducted to yield concentrations of elemental iron in the range from 3 wt% to 10 wt% in the finale ceramic composite, expressed on a ceramic yield of the pure PSO compound of 80 wt% as determined by TG. In the case of the ferrocene, resin formulations containing 10 wt%, 20 wt% and 37.5 wt%, also expressed on a ceramic yield of 80 wt% of the pure PSO compound, were investigated. The pyrolyzed samples were labelled as SiOC(xFe) − y, where *x* represents the expected weight percent of elemental iron. The *y* indicates the used precursor by abbreviating ligands as $acac_3$ (acetylacetonate) for the ferric acetylacetonate precursor, or cp_2 (dicyclopentadienyl) in the case of ferrocene. The used labels are listed in Table 1.

Organometallic precursors were first placed in plastic containers in the glovebox, followed by immediate addition of the selected solvent so that the mixture contains a 5:1 wt ratio of solvent to organometallic precursor at ambient conditions. Precursors were dissolved in solvents by magnetic stirring. Afterwards, PSO was added at room temperature, followed by the addition of TPM after 2 hrs. The mixture was stirred at room temperature until all of the solvent (o-xylene or toluene) had evaporated from the system, resulting in an opaque mixture in the case of ferric acetylacetonate, or an orange colored mixture in the case of ferrocene addition. The mass ratio between Fe-modified PSO and TPM solvent was adjusted to enable photocuring of the photosensitive resin. A mass ratio 6:1 = TPM:PSO was required in case of the $Fe(acac)_3$ precursor due to high light absorption, while 1:1 = TPM:PSO was used

Table 1
Sample compositions showing the starting resin formulations and the corresponding sample designations after printing/pyrolysis.

Resin formulation				Printed/Pyrolyzed monoliths
Label	Fe precursor	Fe content* (wt.%)	TPM:PSO	Label
0Fe-acac$_3$	/	0	6:1	SiOC(0Fe)-acac$_3$
3Fe-acac$_3$	Fe(acac)$_3$	3	6:1	SiOC(3Fe)-acac$_3$
5Fe-acac$_3$	Fe(acac)$_3$	5	6:1	SiOC(5Fe)-acac$_3$
7Fe-acac$_3$	Fe(acac)$_3$	7	6:1	SiOC(7Fe)-acac$_3$
10Fe-acac$_3$	Fe(acac)$_3$	10	6:1	SiOC(10Fe)-acac$_3$
0Fe-cp$_2$	/	0	1:1	SiOC(0Fe)-cp$_2$
10Fe-cp$_2$	Fe(cp)$_2$	10	1:1	SiOC(10Fe)-cp$_2$
20Fe-cp$_2$	Fe(cp)$_2$	20	1:1	SiOC(20Fe)-cp$_2$
38Fe-cp$_2$	Fe(cp)$_2$	38	1:1	SiOC(38Fe)-cp$_2$

* Theoretically predicted Fe content in the material after complete pyrolysis, assuming no volatilization of Fe species and the PSO yield of 80 wt%.

for formulations modified with ferrocene. Separately, TEOS was stirred into the TMPTMA solution. In the next step, the Fe-modified PSO/TPM solution was added dropwise to the TEOS/TMPTMA solution, resulting in a low-viscosity liquid. Finally, stabilizing additives and photoinitiator were added before vat photopolymerization. The base photosensitive resin blend consisted of 44 wt% of PSO/TPM, 12 wt% of TEOS, and 44 wt% of TMPTMA [19]. For comparison purposes, neat photosensitive resins were prepared in the same way, without the addition of Fe-based precursors. The mass contents of compounds used for modification of PSO as the weight percentages of the used compounds in 10Fe-acac$_3$ and 38Fe-cp$_2$ photosensitive resin formulations are listed in Table S1.

2.3. Design and 3D printing of SiOC(Fe) structures by vat photopolymerization (VPP)

The utilization of the triply periodic minimal surface (TPMS) has emerged as a highly effective approach for designing lattice structures due to its intricately connected lattice structures, smooth surfaces, and possibility to precisely control geometric properties. Increasingly used TPMS structures as advanced catalyst supports are Schwarz primitive, diamond, and gyroid due to enhanced fluid mixing, more uniform heat distribution and lower pressure drop compared to packed bed reactors [20]. The Schwarz primitive TPMS design has been selected due to reported potential for heat transfer applications and low pressure drop [21]. Hence, the catalyst support design based on a Schwarz primitive TPMS unit cell with a unit length of 5 mm and a wall thickness of 0.5 mm was designed using nTopology software (nTop, USA), as depicted in Fig. 1b. The dimensions of the cylindrical catalyst support were 15 mm for diameter and up to 40 mm for length. In the case of horizontally oriented samples, the supports were generated using DeskArtes 3Data Expert 15.0 software (DeskArtes, Finland). CeraFab Control (Lithoz GmbH, Austria) was used as a slicing software to generate the print file. Printing was conducted on CeraFab 7500 and CeraFab S65 printer systems (both Lithoz GmbH, Austria). Both printers used to fabricate monoliths are DLP-based printers specifically designed for ceramic fabrication. The main difference between the two systems were the available building envelopes (76 × 43 × 150 mm for CeraFab 7500 vs 102 × 64 × 320 mm for CeraFab S65) and the different maximum light intensity which were 80 mW·cm^{-2} and 60 mW·cm^{-2}, respectively.

The printing conditions, such as exposure energy dose and layer height, were determined individually for each resin formulation by light exposure tests. Prior to printing, the resin was ultrasonicated to remove air bubbles, and was poured into the vat. The printed monoliths were removed with a razor blade from the building platform, followed by

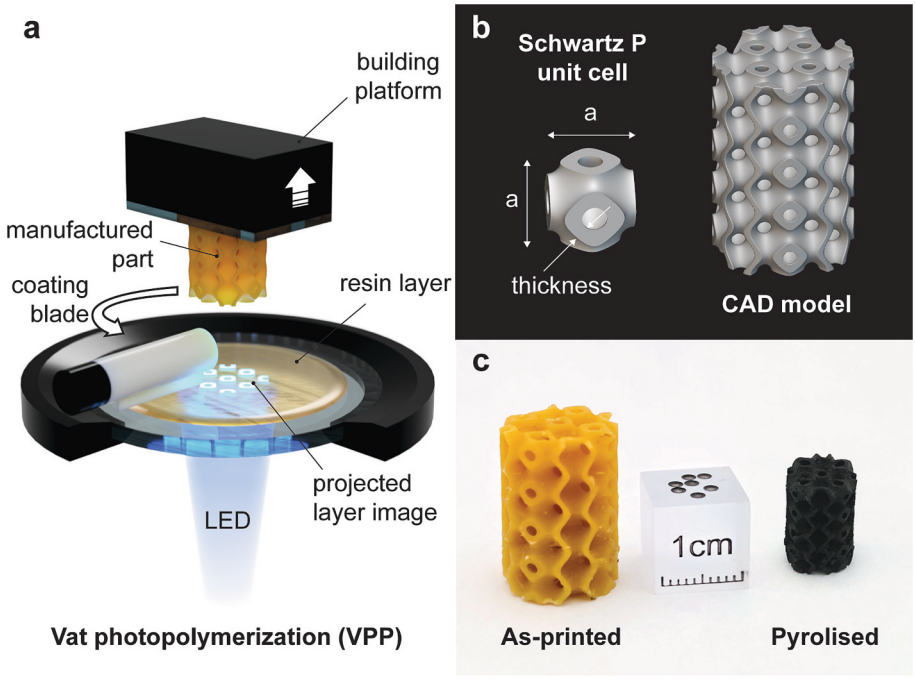

Fig. 1. A) VPP printing process with schematic diagram of the utilized CeraFab S65 printer; b) designed CAD model; c) as-printed and pyrolyzed SiOC(38Fe) – cp$_2$ monolith.

ultrasonic treatment in TPM for 5 min to wash the excess of the uncured resin. Compressed air was used to remove the remaining TPM, and the monoliths were stored in a desiccator for further processing. The pyrolysis of the printed monoliths was conducted in an alumina tube furnace (RHTC 80–450/15, Nabertherm GmbH, Germany) under flowing argon atmosphere of 0.3 $dm^3 \cdot min^{-1}$ by applying a heating rate of 0.5 °C·min^{-1}, including multiple dwell stages to remove the organic components up to maximum temperature, ranging from 600 to 1500 °C, with a dwell time of 2 h. A cooling rate of 2 °C·min^{-1} was applied to ensure shape preservation of the pyrolyzed structures. Before pyrolysis, the monoliths were placed on a carbon felt which was positioned at the bottom of an uncovered alumina crucible.

2.4. Characterization

The photopolymerization test under blue light with a wavelength of 460 nm was first conducted to determine the cure depth and the exposure intensity of the photosensitive resins in order to set printing parameters. The maximum light intensity was applied in distinctive time durations to determine the optimal energy dose by exposing three circular shapes per energy dose. A maximum energy dose of 3000 mJ·cm^{-2} was achieved by exposing the photosensitive resin to a light intensity of 80 mW·cm^{-2} for a duration of 37.5 s using the CeraFab 7500 system. An analogous approach was applied for resins with a ferrocene precursor by using CeraFab S65, where a maximum energy dose of 1000 mJ·cm^{-2} was achieved by emitting a light intensity of 60 mW·cm^{-2} for a duration of 16.7 s. The thickness of the cured layer was then measured using a micrometre screw gauge C110T (Kroeplin GmbH, Germany). The ceramic conversion of the photosensitive resin and the 3D-printed green bodies were monitored by thermogravimetric analysis (STA 449C Jupiter, Netzsch, Germany) under 50 $cm^3 \cdot min^{-1}$ argon flow by applying heating ramp of 5 K·min^{-1} from 30 to 1500 °C for all measurements, the sample amount being around 30 mg. Additionally, ceramic yield and the linear shrinkage were determined with an analytical balance and a sliding gauge, respectively. The chemical composition of the Fe-modified resins was analyzed by Fourier-transform infrared spectroscopy (FTIR; Perkin Elmer Spectrum 100, USA), with a measuring range from 400 to 4000 cm^{-1} at a resolution of 4 cm^{-1}. The phase composition of the pyrolyzed structures was analyzed by a high-resolution X-ray powder diffractometer X'Pert PRO MPD (Malvern Panalytical, UK) using $CuK_{\alpha\ 1,2}$-radiation at a diffraction angle 2θ between 10° and 95°.

The macrostructure and morphology of printed and pyrolyzed structures were recorded by an ultra-depth-of-field microscope (VHX-5000, Keyence, Japan). The microstructure of the pyrolyzed ceramics was observed using a scanning electron microscope (Helios NanoLab NL650, FEI, USA). The structure of the magnetic nanoparticles was characterized with a scanning transmission electron microscope (Spectra 300, Thermo Fisher Scientific, Netherlands) at 200 kV accelerating voltage. STEM images were simultaneously recorded with a high-angle annular dark-field (HAADF) and a bright-field (BF) detector. Elemental composition was determined with a Super-X EDS detector with a 4-windowless detector. Acquisition and post-processing data analysis were managed with Velox software. The particle-size distribution of MNPs was determined by manual TEM image analysis of approximately 100 particles. An energy-dispersive X-ray fluorescence spectrometer (EDXRF) was used to determine the Fe content in the pyrolyzed samples by utilizing our in-house-developed QAES (Quantitative Analysis of Environmental Samples) software. Surface area and porosity characteristics of printed and pyrolyzed monoliths were determined from nitrogen adsorption/desorption isotherms at liquid-nitrogen temperature using a Nova2000e instrument (Quantachrome Nova 2000e, Anton Paar QuantaTec Inc., USA). The samples were previously degassed over night at 110 °C in a vacuum. The surface area was determined using the Brunauer-Emmet-Teller (BET) equation with nitrogen-adsorption data in the p/p_0 range between 0.05 and 0.3. Pore size and pore volumes were derived from the desorption curve of the isotherms using the Barrett–Joyner–Halenda (BJH) model. Pore opening diameters and pore size distributions were evaluated by mercury intrusion porosimetry (Pascal 140/440, Thermo Scientific) with a maximum applied intrusion pressure of 400 MPa within the pore size (diameter) interval 3.2 nm to 50 μm. The surface tension and the contact angle of the mercury were set to 0.485 mN·m^{-1} and 130°, respectively. The type of carbon phases was analyzed with a Raman spectrometer (RMS, PerkinElmer, Inc., USA) from powdered samples using an NT-MDT Spectra assembly, with 488 nm excitation light at a power of 5 mW. The spectra were acquired over 50 s by integrating consecutive 0.5 s acquisition intervals. Room-temperature magnetization curves were recorded with a Vibrating-Sample Magnetometer (VSM, Series 8600, LakeShore, USA) from the powdered samples. The specific absorption rate (SAR) of the samples was determined from the magnetic losses recorded during magnetization measurements under alternating magnetic fields (Manyetic®, Nanotech Solutions, Spain), where the SAR value was obtained by multiplying the magnetic area by the employed field frequency of 234 kHz. Magnetic heating of the samples was carried out under alternating magnetic field (AMF) that was generated using a high-frequency generator (Ultraflex HS − 4 W) and a copper tube coil with 7 turns having an inner diameter of 45 mm and a height of 50 mm. The resonant circuit consisting of a capacitor and a copper tube coil was water cooled using a closed compressor cooler (Julabo FL1701). The monolithic catalyst support was fixed between two quartz wool plugs and an N-type thermocouple (Tenma, Japan) was inserted into the central part of the catalyst support during quartz tube placement through copper coil and fixed into apparatus setup. All measurements were performed with nitrogen flowing (30 $cm^3 \cdot min^{-1}$) through the catalyst support while the temperature was continuously monitored. After the room temperature stabilization, a magnetic field with a magnetic field strength of 60 kA·m^{-1} was generated at 214 kHz frequency, and the temperature increase of the catalyst support was acquired in the form of a heating curve (see Fig. S1, Supporting Information).

3. Results and discussion

3.1. Fe-modification of preceramic polymer

The modified PSO mixtures were investigated by FT-IR spectroscopy to investigate the formation of Si–O–Fe bond. The spectra of pure PSO, used solvent and Fe-based precursor were included for comparison purposes (Fig. 2). The transmission bands at 1270 cm^{-1}, 1112 cm^{-1}, 1012 cm^{-1}, 860 cm^{-1}, and 761 cm^{-1}, corresponding to vibrations of Si-CH_3, Si-O-Si, Si-O-C, O–Si–CH_3 and Si-CH_3, respectively, were observed for the pure PSO which is in a good agreement with literature sources [22,23]. The bands in the range from 1510 to 1450 cm^{-1} were associated with aromatic ring stretching for o-xylene, while the aromatic C-H out of plane band was overlapping with Si-CH_3 interaction [24]. The PSO modified with $Fe(acac)_3$ showed the presence of all characteristic bands of pure PSO, indicating that the polymer backbone has been preserved after modification [25]. The registered transmittance bands at 1568 cm^{-1} (C=O), 1519 cm^{-1} (C=C), 1420 cm^{-1} (C–O) and (C–C) at 930 cm^{-1} were corresponding to $Fe(acac)_3$ ligands, as marked in Fig. 2a. The transmittance bands at 665 cm^{-1} and 434 cm^{-1} are identified as (Fe-O) vibrational peaks of $Fe(acac)_3$. Although, a formation Si–O–Fe bonds by condensation reaction between $Fe(acac)_3$ and the silanol groups of the PSO chain has been expected [26,27] such chemical modification wasn't confirmed due to absence of new transmittance bands. Furthermore, the –O–Si–CH_3 bond is still present in the 10 wt% Fe modified PSO furtherly indicating lack of condensation reaction.

The characteristic transmission bands of ferrocene were observed at 1405 and 1103 cm^{-1} ν_{as}(C=C), 1000 cm^{-1} ν_{as}(β(C–H)), 818 cm^{-1} ν_{as}(C–H), and 475 cm^{-1} $\nu_{as}(Fe\pi_6)$, $\nu_{as}(\pi_6\pi_6)$ as visible in Fig. 2b [28]. By comparing transmission bands of individual components with those of the PSO sample modified with ferrocene, it is visible that all individual bands are preserved without the appearance of new transmission bands.

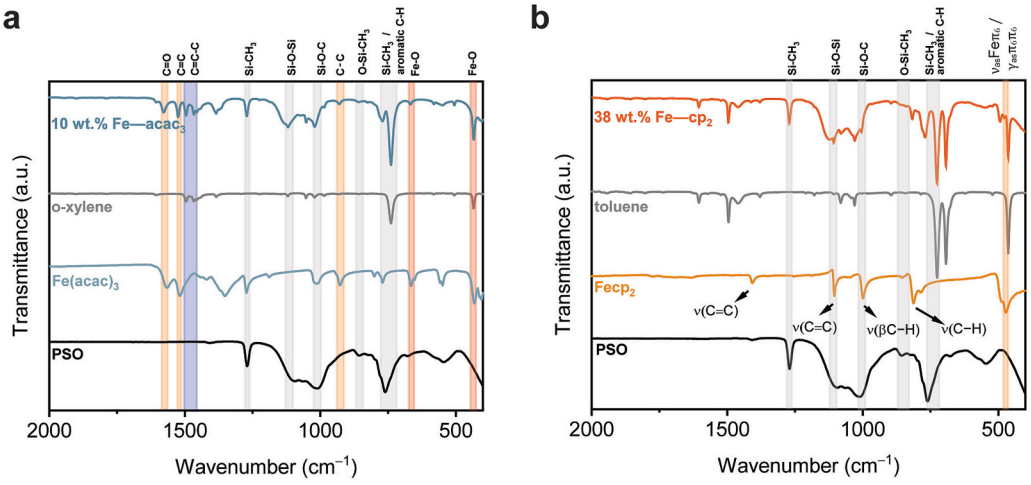

Fig. 2. FTIR spectra of the modified PSO by a) ferric acetylacetonate or b) ferrocene as Fe-based precursor.

Although, the –O–Si–CH_3 bond disappeared, the expected transmittance peak of the Si–O–Fe bond around 950 cm^{-1} wasn't observed [29]. The absence of Si-O-Fe peak indicates that most probably limited or no reaction between Fe-based precursors and PSO occurred at room temperature (Fig. 2b).

3.2. *Setting printing parameters for iron modified PSO's*

The optimal level of energy required to print the samples was determined by measuring the curing depths of the photocurable suspension as shown in Fig. 3a and b. The curing depth is negatively affected by the increasing content of ferric acetylacetonate precursor due to increased opaqueness of the resin which reduces UV/VIS light penetration by absorption and light scattering (Fig. 3c). Mitteramskogler et al. [30] reported that the curing depth should be approximately three times higher than the thickness of the printed layers to mitigate crack formation during the thermal post-processing. Hence, the parts generated in this study using $Fe(acac)_3$ as precursor were printed with a layer thickness of 20 μm and an energy dose of 1200 $mJ{\cdot}cm^{-2}$, except for the parts generated from photosensitive resin containing 3 wt% Fe, where an energy dose of 600 $mJ{\cdot}cm^{-2}$ was applied. Even though the applied energy dose of 1200 $mJ{\cdot}cm^{-2}$ did not meet the aforementioned recommendation for all formulations tested, the printed parts were undamaged and printed faster than it would be with higher energy doses. Catalyst supports fabricated from resin formulations containing more than 3 wt% of Fe were printed in horizontal position with generated supports (Fig. S2, Supporting Information). The reasoning was to expedite the printing process and prevent premature gelation of the resin, which occurred in formulations with higher Fe content in prolonged experiments (e.g., printing in a vertical position). The presence of metal ions in the photosensitive resin formulation could reduce the activation energy of double bonds [31], which, in combination with light scattering during the printing process, resulted in gelation of the resin. Hence, based on the measured curing depths and observed resin stability, a maximum iron content of 10 wt% was achievable when Fe $(acac)_3$ was used as Fe precursor.

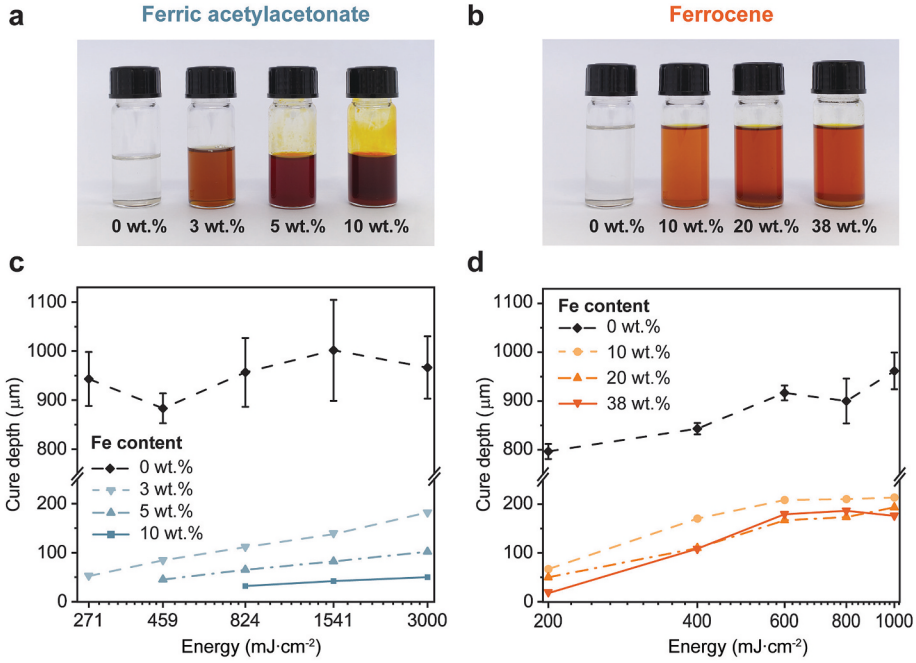

Fig. 3. Iron modified PSO resin formulations with increasing content of Fe precursor a) from 0 wt% to 10 wt% Fe – $acac_3$ and b) from 0 wt% to 38 wt% Fe – cp_2. The measured cure depths as a function of energy dose c) up to 10 wt% Fe – $acac_3$ and d) up to 38 wt% Fe – cp_2.

When using ferrocene as an Fe precursor in the photosensitive resin formulation, satisfactory curing depths were achieved even with a maximum content of Fe up to 38 wt% (Fig. 3d), which corresponds to a 1:1 wt ratio between preceramic polymer and ferrocene. This allowed the preparation of photosensitive resins with a decreased TPM solvent content (PSO:TMP = 1:1), and an increased PSO content. An energy dose of 700 mJ·cm^{-2} and a layer height of 50 μm were selected to fabricate catalyst supports. Even though resin formulations containing ferrocene did not exhibit gelation phenomena even after prolonged printing sessions, precipitations formed at the bottom of containers at increased ferrocene content ≥ 20 wt% Fe – cp_2 (Fig. 3b). A similar behavior was observed in the case of resin formulations containing ferric acetylacetonate ≥ 7 wt% Fe – $acac_3$, albeit much less pronounced due to lower content of the precursor compared to ferrocene formulations (Fig. 3a). Regarding shelf life, both resin formulations demonstrated satisfactory stability and remained printable for a period of 1–2 months when stored under proper conditions (cool, dark environment), with no significant change in viscosity or signs of premature gelation. However, for 20Fe-cp_2 and 38Fe-cp_2 resin formulations, periodic remixing was required to counteract sedimentation.

3.3. VPP printing of SiOC(Fe) monoliths

Cylindrical monoliths based on Schwarz primitive unit cells were successfully printed from resin formulations with various Fe contents, as shown in Fig. 4. The printed parts exhibited smooth surfaces and excellent handleability. The parts show visible cracks on their surface due to pronounced shrinkage. The generation of cracks during the pyrolysis process is influenced by the wall thickness and part shape. In general, additively manufactured complex shapes based on preceramic polymers commonly demonstrate crack formation and considerable porosity due to the release of gaseous products during crosslinking and pyrolysis of the PCPs during the ceramization process [32].

After pyrolysis, a linear shrinkage of 45.5 ± 1 % and a volume shrinkage of 84.2 ± 0.5 % were determined regardless of Fe content in the resin formulations containing $Fe(acac)_3$ as a precursor. As mentioned before, the significant shrinkage resulted in crack formation during the pyrolysis process, with a decrease in structural integrity of the parts with increasing Fe content. The calculated ceramic yield of 13 ± 0.1 % was in good agreement with the one determined from TG curves (Fig. 5.). On the other hand, the resin formulation containing ferrocene as a precursor demonstrated excellent printability, even at significantly higher Fe contents up to 37.5 wt%. Furthermore, the linear shrinkage and volume shrinkage were reduced to 32.4 ± 1.2 % and to 67.8 ± 1.3 %, respectively, resulting in improved structural stability of SiOC(38Fe) – cp_2 parts due to an increased ceramic yield up to 20 wt%. Hence, such monoliths can be used for gas-phase reactions at atmospheric pressure due to their resistance to rapid temperature fluctuations and corrosive environments, whereas higher operational pressures may compromise their structural integrity.

3.4. Ceramization

The polymer-to-ceramic transformation of pure PSO, $Fe(acac)_3$-

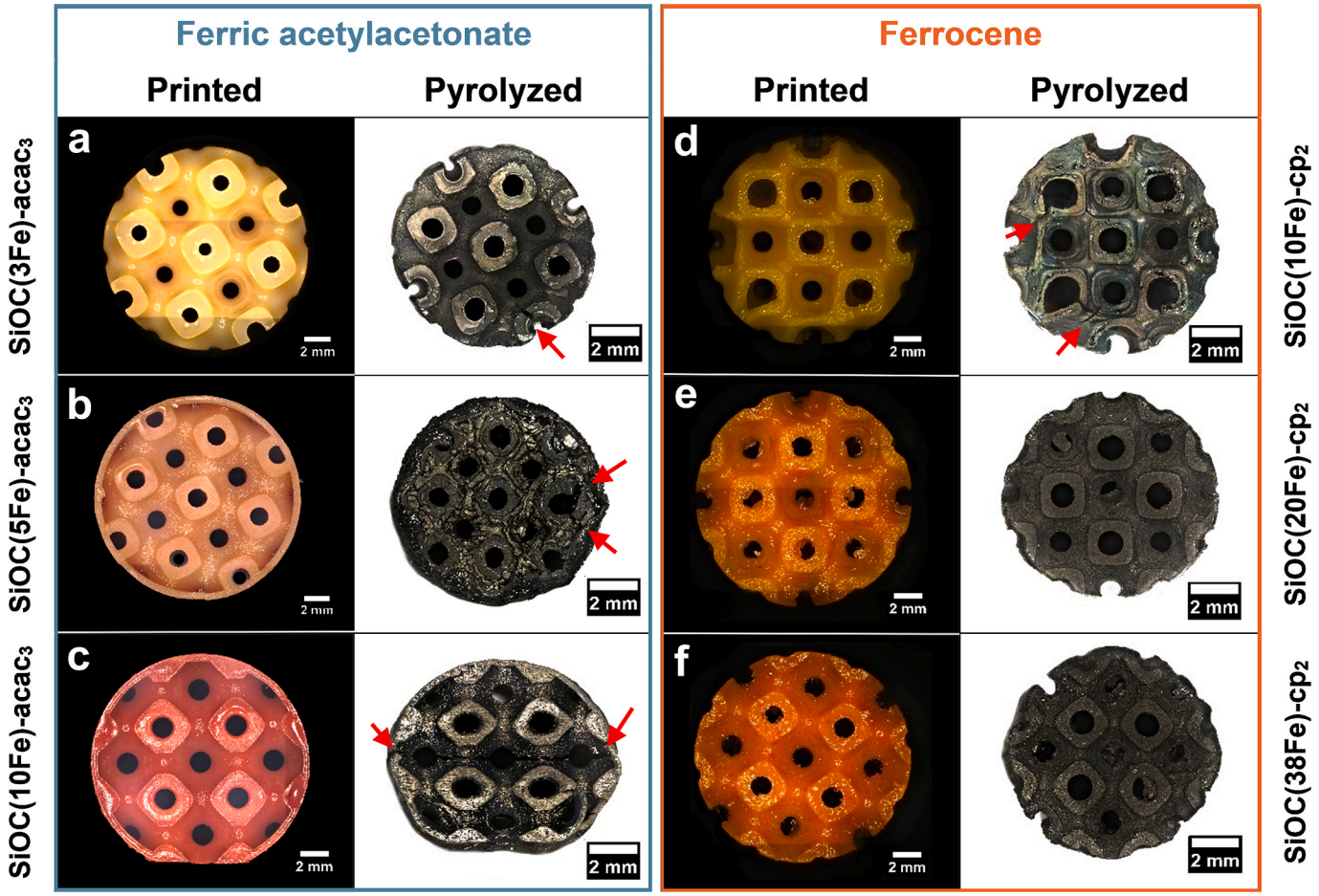

Fig. 4. Macrographs of the SiOC(Fe) ceramics as-printed and after pyrolysis at 900 °C: a)-c) containing $Fe(acac)_3$ as precursor and d)-f) containing $Fe(cp)_2$ as precursor. The red arrows indicate crack formation. The side views of pyrolyzed structures containing the highest Fe contents in their resin formulations are shown in Fig. S3, Supporting Information. (For interpretation of the references to colour in this figure legend, the reader is referred to the web version of this article.)

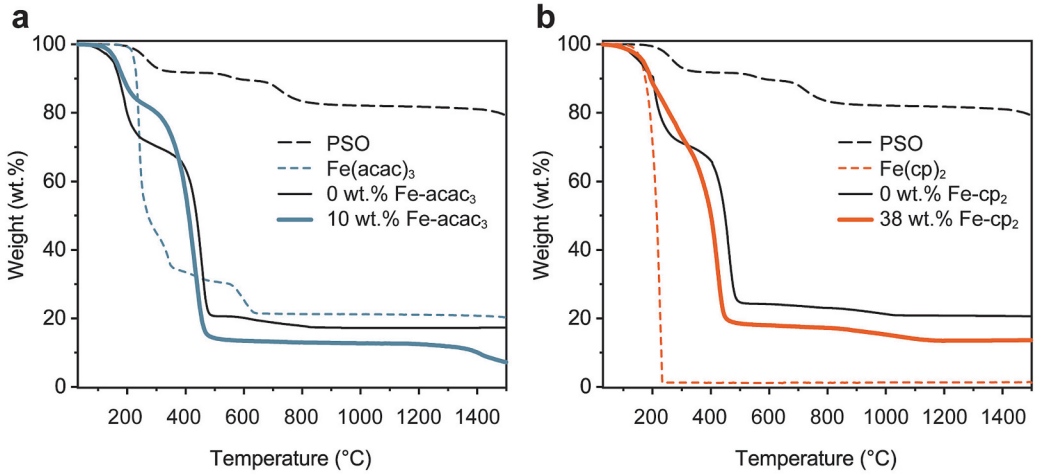

Fig. 5. TG curves of: a) individual components and 10 wt% Fe – $acac_3$ resin, b) individual components and 38 wt% Fe – cp_2 resin, measured up to 1500 °C under argon.

modified PSO and $Fe(cp)_2$-modified PSO was analyzed by TG analysis in the temperature range between room temperature and 1500 °C in argon. In the case of $Fe(acac)_3$-modified PSO, a ceramic yield of approximately 14 wt% was obtained at the pyrolysis temperature of 900 °C. A slightly higher yield of approximately 20 wt% was obtained when $Fe(cp)_2$ was used as Fe precursor. The results of the thermal analysis of major individual components present in the photosensitive resin and PSO modified with different amounts of Fe by utilizing organometallic precursor Fe $(acac)_3$ or $Fe(cp)_2$ are shown in Fig. 5.

The TG analysis of resin formulations based on $Fe(acac)_3$ precursor is shown in Fig. 5a. The thermal decomposition curve of PSO powder showed a mass loss starting at 230 °C connected to the polycondensation reactions during cross-linking, accompanied by the release of gaseous by-products [23]. At temperatures > 350 °C, there is an almost continuous mass loss due to the ceramization decomposition reactions, which ends at approximately 800 °C. Additionally, a ceramic yield of 80 wt% up to maximum investigated temperature of 1500 °C was recorded. The pure ferric acetylacetonate complex in solid state starts to decompose at temperatures > 200 °C with a weight loss of 76 % between 200 and 680 °C. Finally, the photosensitive resin containing $Fe(acac)_3$ as source of Fe with an expected Fe content of 10 wt% exhibited three distinctive mass loss transitions. The first mass loss can be prescribed to the decomposition of monomers and bigger molecules after loss of solvent, followed by the second mass loss step which can be associated with the decomposition of functional groups present on the modified preceramic polymer. A third mass loss step at temperatures exceeding 1250 °C, only observed in case of the Fe-modified material, is presumably due to the carbothermal reduction reactions of Fe species followed by crystallization of the polymer-derived ceramic matrix.

In Fig. 5b, the TG curves of the prepared resin formulation based on the $Fe(cp)_2$ precursor approach are presented. Ferrocene exhibits a significant weight loss due to the lack of chemical bonding and its volatilization at temperatures higher than 100 °C [33]. Consequently, the decomposition of pure ferrocene results in a weight loss of approximately 99 wt% up to 230 °C. The decomposition of ferrocene in the inert gas phase has been reported to be dominated by surface reactions, with the adsorption of ferrocene or its fragments, such as $Fe(C_5H_5)$ and $Fe(C_5H_4)$, on the surface of reactor's inner wall occurring up to 900 °C. Further increase in temperature was reported to lead to the formation of cementite (Fe_3C) and iron surrounded by graphite layers (FeC) [34]. In our case, certain amounts of Fe could be absorbed on to the outer surface or remain within the inner structure of the pyrolyzed monoliths, while the majority of Fe was lost by argon flow and by adsorbing on the tube's inner wall where it could decompose at higher temperatures. The photosensitive resin containing $Fe(cp)_2$ demonstrated a behavior comparable to that of the resin containing $Fe(acac)_3$ regarding the first two mass loss steps. A difference is visible in the third mass loss step, which can be attributed to the increased PSO content in the $Fe(cp)_2$-based resin formulation, and to the less pronounced carbothermal reduction reactions of iron species, leading to an increased ceramic yield of about 18 wt%. In general, the recorded ceramic yields of Fe-modified resin formulations at 900 °C ranged from 11 wt% to 14 wt% in case of the $Fe(acac)_3$ precursor, and from 15 wt% to 20 wt% for the $Fe(cp)_2$ precursor, respectively (Fig. S4).

3.5. Microstructure and porosity evolution

A microscopic evaluation of SiOC(xFe) monoliths pyrolyzed at 900 °C revealed the formation of internal matrix porosity (Fig. 6a and c). The fracture surfaces of SiOC(10Fe)-$acac_3$ and SiOC(38Fe)-cp_2 monoliths reveal an apparently high amount of relatively small pore open diameters across both surfaces of the pyrolyzed monoliths, which is beneficial for catalyst support materials. In this case, hierarchical porosity, combining a high specific surface area with high mass transfer and dispersion of the active catalytic phase is preferred for catalytic applications. The porosity of the reported PDC monoliths was influenced by induced phase separation during the vat photopolymerization process, as described by Essmeister et al. [19]. The acrylate monomers form a rigid network upon light exposure, resulting in a bicontinuous network of acrylates and preceramic constituents (PSO, TPM, TEOS). The subsequent pyrolysis, leading to organic group decomposition and release of gaseous by-products, results in the formation of micro- and mesopores. The surface properties were quantitatively assessed by N_2 physisorption measurements. The nitrogen adsorption/desorption isotherms were indicative of a Type IV isotherm, typical of mesoporous materials (Fig. 6b). The observed hysteresis shape correlates with well-defined, cylinder-like pore channels or agglomerates of approximately uniform spheres [35]. The total mesoporous volume for the Fe-free samples was 0.069 $cm^3 \cdot g^{-1}$. The Fe addition resulted in an increase of the total mesoporous volume, yielding mesopore volumes of 0.121 and 0.110 $cm^3 \cdot g^{-1}$ for SiOC(10Fe)-$acac_3$ and SiOC(38Fe)-cp_2, respectively. Indeed, the presence of mesoporosity was confirmed by interpretation of the desorption branch via the BJH method, yielding mesoporosity of about 4 nm in size (Fig. S5). With respect to surface area, the Fe-free monolith exhibited a moderate surface area of 17.9 $m^2 \cdot g^{-1}$. The SiOC(10Fe)-$acac_3$ material, in contrast, displayed a slightly higher value of 25.6 $m^2 \cdot g^{-1}$, while the SiOC(38Fe)-cp_2 material exhibited a 3-times larger surface area of 60.5 $m^2 \cdot g^{-1}$, even though exhibiting a comparable pore volume. The reported values are in good agreement with the observed collapse of microporosity at higher temperatures (>700 °C) observed in similar

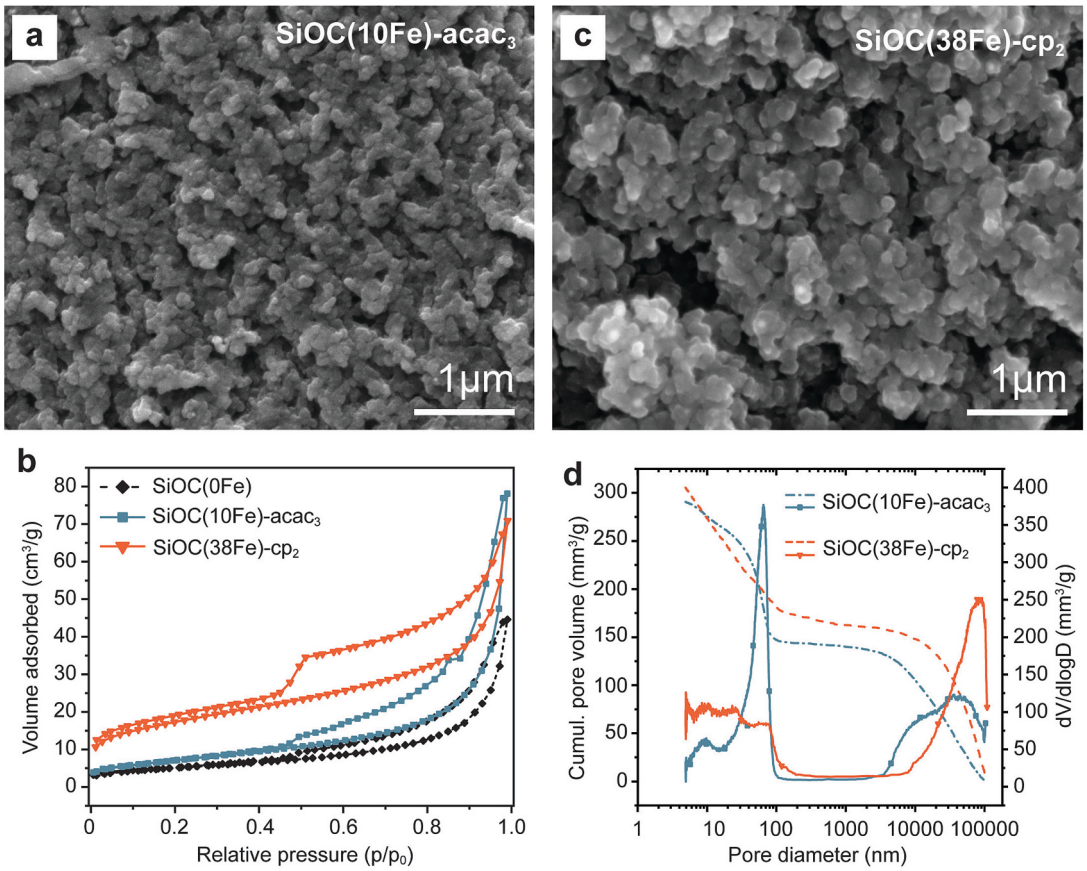

Fig. 6. SEM fracture surfaces of a) SiOC(10Fe)-acac$_3$ and c) SiOC(38Fe)-cp$_2$; b) N_2 isotherms and d) cumulative and differential pore size distributions obtained by mercury intrusion porosimetry.

PDC composites [19]. As expected, the phase separation induced the evolution of mesoporosity, which is visible from the adsorption gain in the range of p/p_0 around 1, indicating a higher pore volume with the presence of bigger pores as confirmed by the pore size distributions.

The bulk properties of SiOC(10Fe)-acac$_3$ and SiOC(38Fe)-cp$_2$ monoliths pyrolyzed at 900 °C, as determined by mercury intrusion porosimetry, yielded comparable results. The monoliths exhibited a bulk density of approximately 1.1–1.2 g·cm^{-3}, exhibiting accessible porosity of ~ 35 % (Table S2). As can be seen from the pore size distribution diagram (Fig. 6d), the samples exhibit trimodal, hierarchical porosity in the meso- and macropore range which can be observed as modal peaks. The mean size of mesopores was slightly larger for SiOC(10Fe)-acac$_3$,

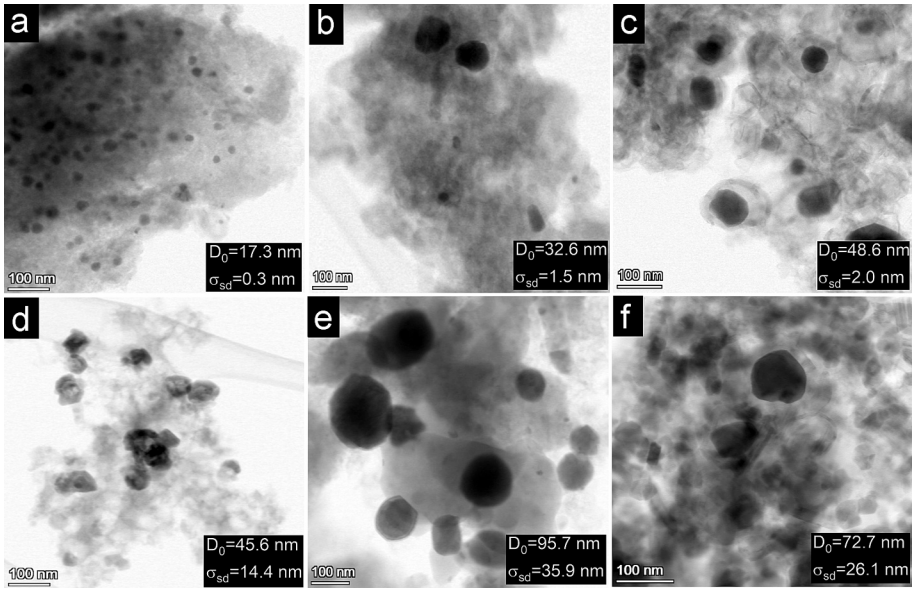

Fig. 7. The *in situ* formation of NPs within the SiOC porous ceramic matrix. TEM micrographs of SiOC(Fe) ceramics pyrolyzed at 900 °C: a-c) SiOC(10Fe)-acac$_3$ and d-f) SiOC(38Fe)-cp$_2$.

while macropores were smaller compared to SiOC(38Fe)-cp$_2$.

3.6. In-situ formation of MNPs

Iron precursors acted as a catalyst driving phase separation and nanocrystal formation during thermal treatment. Regardless of the Fe precursor and the pyrolysis temperature used, nanoparticles were homogeneously distributed within the SiOC matrix (Fig. 7). However, distinct differences in the size and distribution of the formed nanoparticles (NPs) were observed depending on the used Fe-based precursor. In the case of ferric acetylacetonate, NPs demonstrated a narrower particle size distribution with a smaller average particle size and generally higher homogeneity (Fig. 7a-c) compared to NPs obtained by using ferrocene (Fig. 7d-f). For Fe(acac)$_3$, the mean particle size of NPs increased with increasing temperature from 17.3 ± 0.3 nm at 900 °C to 48.6 ± 2 nm at 1500 °C. On the other hand, in the case of ferrocene samples, the growth of MNPs exhibited a less regular trend. The NPs initially increased in size from 45.6 ± 14.4 nm at 900 °C to 95.7 ± 35.9 nm at 1200 °C; a slight decrease in size to 72.2 ± 26.1 nm was determined after pyrolysis at 1500 °C. The decrease in NP size at 1500 °C may result from a phase change, which will be discussed in the context of phase composition development. The absence of carbon nanotubes in the TEM images can be attributed to the pronounced depletion of free carbon by the relatively high iron content, which favors the formation of cementite and subsequently iron silicides, thereby inhibiting the growth of carbon nanotubes [36].

After pyrolysis, PSO structures modified with Fe precursors remain amorphous up to 800 °C (Fig. S6). For samples containing Fe(acac)$_3$ pyrolyzed at 900 °C, there is a broad peak in the X-Ray diffractograms at $2\theta = 23°$, corresponding to the (100) crystal plane of the SiO_2 phase (PDFC Card No. 29–0085), accompanied by prominent diffraction peaks at 2θ ≈ 44.7°, 65.0°, and 82.5°, corresponding to the [110], [200], and [211] planes of Fe (PDFC Card No. 4–28-4563). The lack of Fe peaks in the case of ferrocene can be attributed to the lower Fe content resulting from the large volatilization of ferrocene (Fig. 5b), which yields a significantly lower Fe content than theoretically predicted. Even though Fe peaks were not observed in the case of Fe(cp)$_2$-containing samples pyrolyzed at 900 °C, the presence of Fe-based MNPs was confirmed by TEM. The elemental mapping confirmed a homogeneous distribution of Fe-containing NPs in the surrounding SiOC matrix (Fig. 8c and d), regardless of the used Fe-precursor. In the case of ferrocene, oxygen was also detected in NPs, which was confirmed also by electron diffraction. Bands corresponding to Fe, Fe_2O_3 and SiO_2 were discerned (Fig. S7).

During the temperature increase up to 1200 °C, the formation of iron carbide (Fe_3C) and iron silicides (Fe_xSi_y) was observed. The observed peaks at angles 2θ ≈ 44.7°–45.3° could be assigned to either FeSi or Fe_3Si while the remaining peaks closely match the pattern of α-Fe, however, according to TEM analysis, the NPs contained minor amounts of Si. In the case of Fe(acac)$_3$ precursor, the NPs contained 90 at. % of Fe and 10 at. % of Si and in the case of Fe(cp)$_2$, 80 at. % of Fe and 20 at. % of Si, respectively. Hence, the XRD peaks were labelled as Fe_xSi_y due to the formation of a substoichiometric intermetallic compound with various proportions of Fe and Si. In the literature, the formation of Fe_xSi_y from Fe-containing PCP has been proposed by two distinct pathways: *i*)

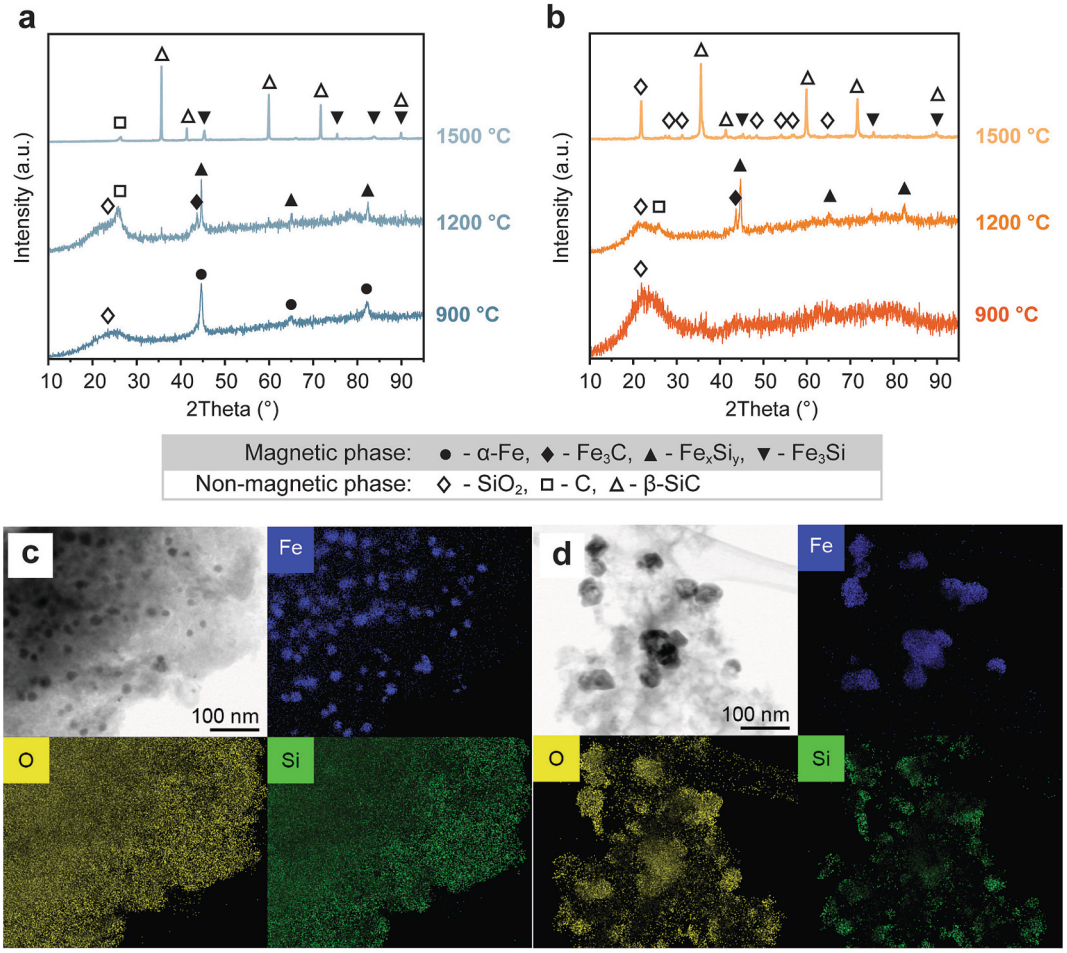

Fig. 8. XRD patterns of SiOC(Fe) after pyrolysis at different temperatures: a) SiOC(10Fe)-acac$_3$ and b) SiOC(38Fe)-cp$_2$. TEM images and elemental mapping of the MNPs obtained after pyrolysis at 900 °C: c) SiOC(10Fe)-acac$_3$ and d) SiOC(38Fe)-cp$_2$. Elemental mapping of pyrolyzed monoliths at higher investigated temperatures is shown in Fig. S9, Supporting Information.

carbothermal reduction of iron oxides to iron, which in return reacts with the SiOC matrix to yield Fe_xSi_y, or *ii*) intermediate formation of an Fe_3C/SiOC nanocomposite, which readily converts to Fe_xSi_y/SiOC [13]. The presence of the Fe_3C phase was confirmed in the diffraction patterns at 1000 °C and 1100 °C (Fig. S6), while at 1200 °C, only one prominent peak remains at 43.7° for both Fe precursors. According to Xu et al. [37], this peak can be assigned to the Fe_3C phase (PDFC Card No. 63–0040).

Pyrolysis temperatures ≥ 1300 °C resulted in the appearance of cubic silicon carbide (PDFC Card No. 29–1129, Fig. 8a and b) in all samples. As SiOC can decompose into multiple amorphous phases SiO_2/SiC/C [26], β-SiC can nucleate from the amorphous SiC phase or through a chemical reaction between SiO_2 and C accompanied by the release of CO, a process that typically occurs at around 1400 °C [36]. According to the literature, the addition of Fe-containing species to PDC promotes the β-SiC formation at slightly lower temperatures [38]. In case of the Fe $(cp)_2$ precursor, a distinct SiO_2 peak at 21.9° was also observed after pyrolysis at 1500 °C. High volatilization of $Fe(cp)_2$ during thermal treatment [39] most likely results in insufficient C content to react with SiO_2 to SiC by carbothermal reduction. In the case of $Fe(acac)_3$, free carbon peaks were observed at $2\theta \approx 26°$. Additionally, the presence of free carbon and its graphitization with increasing temperature was further confirmed by Raman spectroscopy (Fig. S8, Table S2).

The observed phase development of SiOC(Fe) under argon atmosphere is in a good agreement with previous studies where the phase separation of the amorphous SiOC matrix into SiO_2, free C, and FeO_x occurs at lower temperatures (<900 °C) [40]. By further temperature increase (>1200 °C), the formation of a β-SiC phase was observed due to the carbothermal reaction between SiO_2 and C. FeO_x species were reduced to α-Fe and metastable Fe_3C, which reacted with the SiOC matrix at > 1100 °C, resulting in the formation of iron silicide phases [26,41]. Although Fe-containing nanoparticles readily oxidize when exposed to ambient conditions, no iron oxide peaks were observed in the XRD patterns regarding SiOC(10Fe)-$acac_3$, indicating that the MNPs were well protected from oxidation by encapsulation within the SiOC matrix. In the case of SiOC(38Fe)-cp_2, the presence of hematite (Fe_2O_3) was observed (Fig. S7). Due to the lack of chemical modification, ferrocene formed a simple blend with PSO. As NPs were formed, they were less embedded in the SiOC matrix and, as such, more exposed to the environment and more readily oxidized.

3.7. Magnetic heating of the monoliths with embedded MNPs

The magnetic properties of pyrolyzed monoliths were investigated to verify their applicability for magnetic heating in a catalytic process. The magnetic properties were investigated at room temperature after pyrolysis of the printed structures (Fig. 9).

The mass magnetization per amount of sample, reflecting the total composition including non-magnetic phases, changes with pyrolysis temperature due to the formation of Fe/Fe_3C MNPs at lower temperatures, followed by the formation of various iron silicide phases within the SiOC matrix at higher temperatures. The hysteresis loops of the SiOC (10Fe)-$acac_3$ and SiOC(38Fe)-cp_2 samples show modest values of saturation magnetizations, consistent with the rather low amount of incorporated magnetic phases (Fig. S9, Table 3). Because Fe is the only

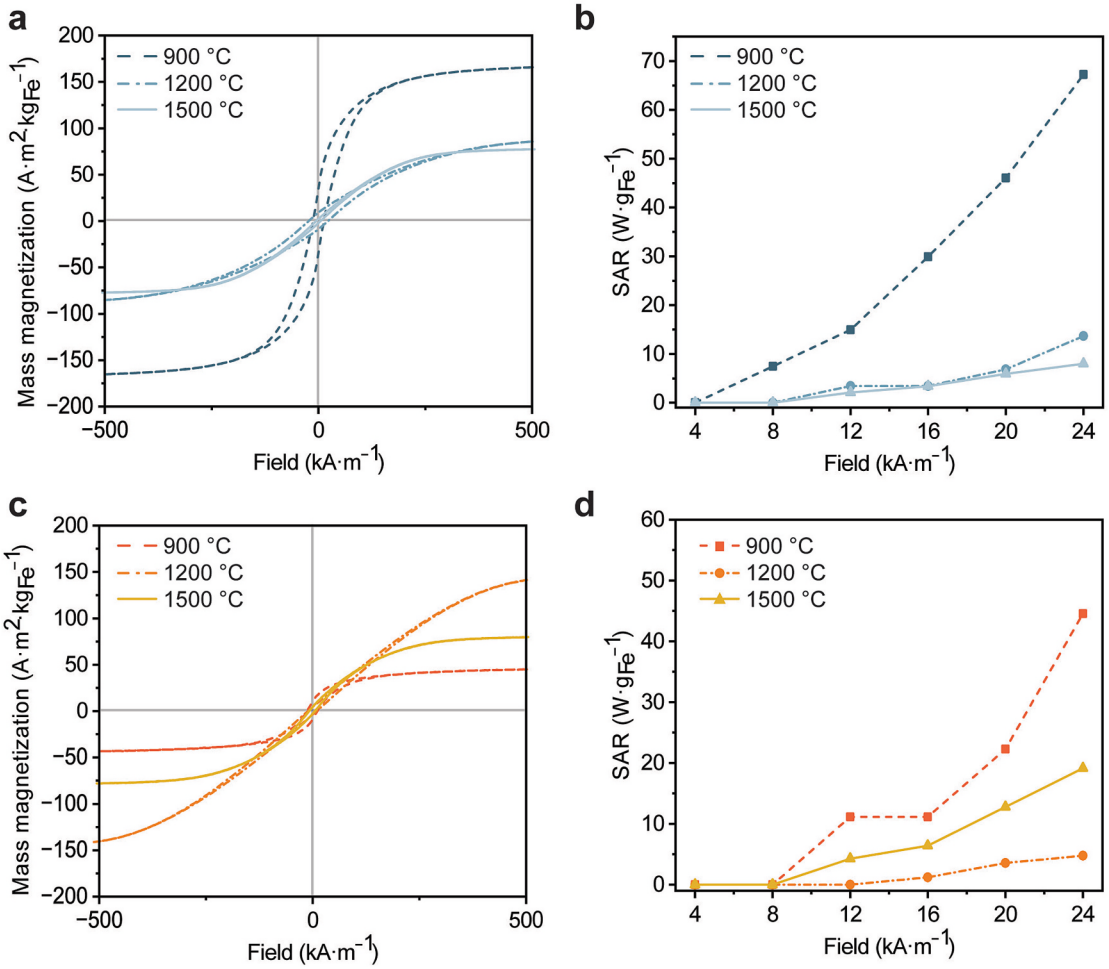

Fig. 9. Room-temperature magnetic hysteresis loops (zoomed in) of: a) SiOC(10Fe)-$acac_3$ and c) SiOC(38Fe)-cp_2 monoliths pyrolyzed at various temperatures. Specific absorption rate (SAR) dependence on the AMF amplitude (H) measured at 234 kHz: b) SiOC(10Fe)-$acac_3$ and d) SiOC(38Fe)-cp_2.

Table 3
Properties of the *in situ* formed MNPs at different pyrolysis temperatures of SiOC(Fe) monolithic structures.

Sample	Pyrolysis temperature, °C	MNP composition	Particle size[a], nm	Fe content [b], wt.%	SAR [c], W g_{Fe}^{-1}	Achieved temperature [d], °C
SiOC(10Fe)-$acac_3$	900	α-Fe	17.3 ± 0.3	3.03 ± 0.4	67.2	192
	1200	Fe_xSi_y	32.6 ± 1.5	2.49 ± 0.3	13.7	169
	1500	Fe_3Si	48.6 ± 2.0	7.90 ± 0.9	8.0	128
SiOC(38Fe)-cp_2	900	α-Fe	45.6 ± 14.4	0.9 ± 0.1	44.6	145
	1200	Fe_xSi_y	95.7 ± 35.9	2.8 ± 0.3	4.8	129
	1500	Fe_3Si	72.7 ± 26.1	1.6 ± 0.2	19.2	146

[a] Determined from TEM images by applying a normal distribution curve; [b] Determined by using an energy-dispersive X- ray fluorescence spectrometer (EDXRF); [c] Measured at 24 kA·m^{-1}; 234 kHz; [d] Measured at 60 kA·m^{-1}; 214 kHz.

magnetic element present in all the magnetic phases, the saturation magnetization normalized per amount of Fe reflects the composition of the magnetic phases present in the sample. For the SiOC(10Fe)-$acac_3$ and SiOC(38Fe)-cp_2 samples pyrolyzed at 900 °C, 1200 °C, and 1500 °C, the dependence of mass magnetization (M) on the applied field (H) is presented in Fig. 9a and c. The recorded curves exhibit small values of coercivity and remanence typical for soft ferromagnetic materials. Among all samples, only SiOC(10Fe)-$acac_3$ pyrolyzed at 900 °C exhibits a magnetization curve with high magnetic susceptibility, while the other material variants show slanted curves characteristic for materials with a low value of magnetic susceptibility. Saturation magnetization of the SiOC(10Fe)-$acac_3$ at 900 °C is 170 A·m^2·kg^{-1}, which is lower than the value for bulk α-Fe (217.9 A·m^2·kg^{-1}), [42] indicating that some of the Fe is present in the form of a paramagnetic compound (e.g., FeO, formed by exposure of samples to air atmosphere). For the rest of the samples, the magnetization curves indicate that the main fraction of ferromagnetic phases present are Fe silicides, as both α-Fe and magnetic iron oxides (which could form by oxidation of Fe nanoparticles when samples are exposed to air atmosphere) would display higher susceptibilities.

Fig. 9b and d show the evolution of SAR with AMF amplitude for SiOC(Fe) samples after varying pyrolysis temperature. SAR values reported here are a product of frequency and dynamic hysteresis loop area. For nanosized magnetic particles, this so-called magnetic heating is the predominant heating mechanism. In contrast, larger, micron-sized particles predominantly heat due to so-called induction heating, driven by eddy currents induced by AMF within particles [43]. Both samples pyrolyzed at 900 °C were composed mostly of α-Fe as a magnetic phase, thus exhibiting the highest values of SAR normalized per amount of Fe. Also, the SAR evolution with AMF shows a power law-like increase consistent with the Stoner–Wohlfarth-derived model [44]. All other samples are characterized by slanted, low-susceptibility magnetization curves, meaning that at low AMF amplitudes their magnetization reaches only a small value. As a result, dynamic hysteresis loops are of lower area and, consequently, lower SAR per amount of Fe as well.

The SiOC(Fe) catalyst supports were tested in a laboratory setup to determine their magnetic heating by determining the steady-state temperature, which is the temperature that the material reaches when it stabilizes under the applied AMF. Even though the steady-state temperature is a very important property of the system for magnetic-assisted catalysis, it should be noted that it depends not only on the heating ability or intrinsic magnetic properties of the material, but also on the properties of the measuring setup such as dimensions of the reactor, insulation, the gas flow rate, thermal conductivity, and thermal capacity of the involved materials which directly affects the achieved steady-state temperature. The steady-state temperatures reached by the SiOC(Fe) samples pyrolyzed at 900 °C, 1200 °C, and 1500 °C were measured at 214 kHz frequency with pyrolyzed monoliths under nitrogen flowing through the quartz tube at 30 cm^{-3}·min^{-1} at magnetic field strength of 60 kA·m^{-1}. The results are shown in Fig. 10.

As expected from SAR values (Table 3) and a relatively large amount of incorporated Fe (3.03 wt%), the best heating performance was determined for the SiOC(10Fe)-$acac_3$ sample pyrolyzed at 900 °C (Fig. 10a). This sample reached approximately 200 °C within 3 min. Both other samples from this group reached lower temperature, consistent with their lower SAR values. In the case of SiOC(38Fe)-cp_2 samples, the highest temperature reached was by samples pyrolyzed at 900 °C and 1500 °C (Fig. 10b). Samples pyrolyzed at 900 °C showed the highest SAR per amount of Fe; however, a higher amount of incorporated Fe in the sample pyrolyzed 1500 °C compensates for its lower SAR value per amount of Fe. The sample pyrolyzed at 1200 °C shows the smallest SAR value per mass of sample, and consequently the steady-state temperature is lowest. All the samples reached relatively high temperatures which are appropriate for low-temperature catalytic reactions such as degradation of organic dyes in water purification systems

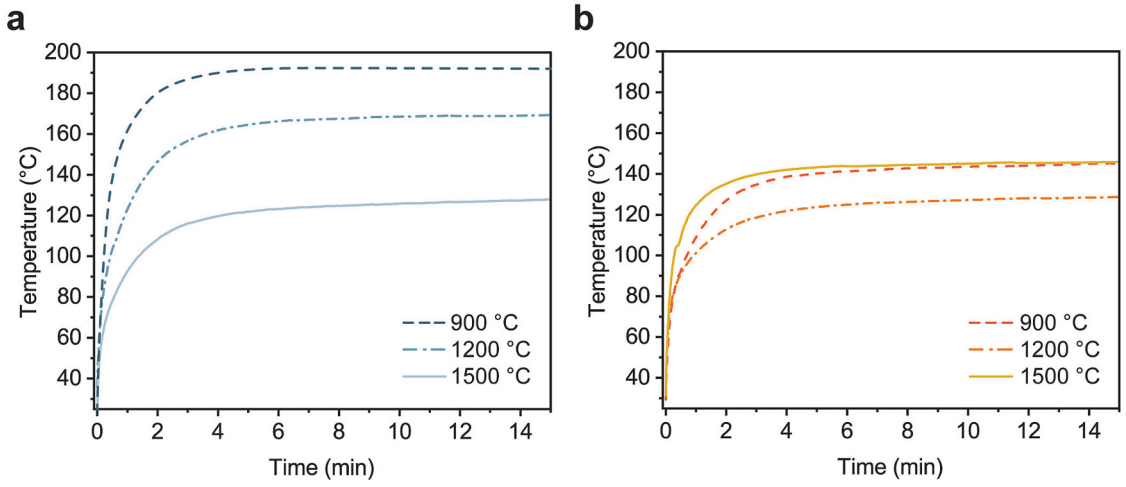

Fig. 10. Steady-state temperatures achieved within SiOC(Fe) monoliths pyrolyzed at different temperatures: a) SiOC(10Fe)-$acac_3$ and b) SiOC(38Fe)-cp_2 (measured at 60 kA·m^{-1}; 214 kHz).

[45], or various hydrogenation reactions involving compounds such as acetophenone [46] and benzaldehyde [47]. The heating performance is governed by the SAR, which increases with the amplitude of the alternating magnetic field. In the low-field regime SAR scales approximately quadratically with field amplitude, while at higher fields this dependence weakens as magnetic saturation is approached. Static hysteresis measurements indicate that the sample approaches saturation only above ~ 300 kA·m^{-1}, whereas the maximum field applied in this study was 60 kA·m^{-1}. This suggests that the observed temperature of around 200 °C is not an intrinsic material limit, but rather a consequence of the available field strength. Higher temperatures could therefore be achieved at higher field amplitudes or increased magnetic nanoparticle loading. The implementation of magnetically heated, catalytically active monoliths results in bypassing the need to heat an entire gas or liquid volume, which leads to rapid temperature response times. Additionally, rapid on/off magnetic heating enables switching a catalytical process on and off on-demand, which makes it a solution compatible with the intermittent nature of renewable energy sources like solar and wind power [48,49].

4. Conclusion

In this work, we demonstrated the development of multifunctional polymer-derived ceramic nanocomposites. Fe-modified PCPs were used to successfully prepare photosensitive resins suitable for DLP process. The ceramization of 3D printed monoliths led to an *in situ* formation of MNPs, which enabled their controlled heating when exposed to an alternating magnetic field.

Modification of PSO with ferrocene enabled a significantly higher iron content in the resin formulation compared to Fe(acac)$_3$, which was limited due to reduced cure depths. The monoliths exhibited bulk density of approx. 1.1–1.2 g·cm^{-3}, showing accessible porosity of ~ 35 % and trimodal, hierarchical porosity, including meso- and macropores, regardless of the used Fe precursor after pyrolysis at 900 °C. The magnetic response depends on the phase composition and the size of the *in situ* formed MNPs, which are primarily related to the pyrolysis temperature. Promising magnetic properties of pyrolyzed SiOC(Fe) originate from Fe/Fe$_3$C obtained at lower temperatures with smaller MNP size, while at temperatures ≥ 1200 °C, the formation of various iron silicide phases with noticeable increase in MNP size was observed. The phase development for each used precursor was very similar, with slight differences at the highest investigated temperature. Based on X-ray diffraction analysis, in case of ferrocene, pronounced SiO_2 patterns and a lack of C patterns were noticed. Furthermore, the average particle size of the generated MNPs was higher in the case of monoliths containing ferrocene as an Fe-based precursor, thus negatively affecting the heating capability. The highest SAR value of 67.2 W·g_{Fe}^{-1} was recorded for SiOC (10Fe)-acac$_3$ monolith pyrolyzed at 900 °C, where nanoparticles of α-Fe with a size of 17.3 ± 0.3 nm were obtained. Samples composed of larger α-Fe and Fe silicide nanoparticles showed significantly decreased magnetic heating capability due to lower magnetic susceptibilities. The subsequent determination of steady-state heating temperatures revealed a maximum temperature of 190 °C achieved within 3 min for SiOC (10Fe)-acac$_3$, while a maximum temperature of approximately 140 °C was achieved for SiOC(38Fe)-cp$_2$.

Demonstrated by these results, the proposed approach of fabricating monoliths with magnetic heating capability is highly promising, offering a substantial increase in energy efficiency by moving catalysis from bulk heating to precise, on-demand energy delivery. The proposed approach could be further explored, e.g. by incorporating phases with increased magnetic properties in order to increase the achievable working temperature, as well as by limiting the formation of large aggregates during *in situ* formation of MNPs. In this way, the magnetically heated catalyst supports could be utilized in future green energy applications such as hydrogen production via steam methane reforming or by ammonia cracking, both processes of which require higher temperatures.

Funding Sources

This project has received funding from the European Union's Horizon 2020 research and innovation programme under the Marie Skłodowska-Curie grant agreement No 101108281. The Slovenian Research Agency is acknowledged for funding through Research programs P2–0087 by AK and P2-0089 by SG. TK acknowledges funding support by the Austrian Science Fund (FWF): I 6593-N.

CRediT authorship contribution statement

Milan Vukšić: Writing – original draft, Visualization, Validation, Methodology, Investigation, Formal analysis, Data curation, Conceptualization. **Thomas Konegger:** Writing – review & editing, Supervision, Methodology. **Martin Schwentenwein:** Writing – review & editing. **Sašo Gyergyek:** Writing – review & editing, Methodology, Data curation. **Anja Sedminek:** Methodology, Investigation. **Sandra Drev:** Methodology, Investigation. **Marijan Nečemer:** Methodology, Investigation. **Andraž Kocjan:** Writing – review & editing, Methodology, Data curation. **Aljaž Iveković:** Writing – review & editing, Visualization, Validation, Supervision, Methodology, Funding acquisition, Data curation, Conceptualization.

Declaration of competing interest

The authors declare that they have no known competing financial interests or personal relationships that could have appeared to influence the work reported in this paper.

Acknowledgement

The authors thank Dr. Janvit Teržan for his support with steady state temperature measurements. Special thanks to Tobias Felsberger, who performed TG analysis of the reported samples. Further appreciation goes to Robert Fülöp of Wacker Chemie AG and Daniel Röttger of Rahn AG for the provision of chemicals.

Appendix A. Supplementary data

Supplementary data to this article can be found online at https://doi.org/10.1016/j.matdes.2026.116126.

Data availability

Data will be made available on request.

References

[1] W. Wang, G. Tuci, C. Duong-Viet, Y. Liu, A. Rossin, L. Luconi, J.-M. Nhut, L. Nguyen-Dinh, C. Pham-Huu, G. Giambastiani, Induction heating: an Enabling Technology for the Heat Management in Catalytic Processes, ACS Catal. 9 (2019) 7921–7935, https://doi.org/10.1021/acscatal.9b02471.

[2] J.-S. Pavelić, S. Gyergyek, B. Likozar, M. Grilc, Process electrification by magnetic heating of catalyst, Chem. Eng. J. 505 (2025) 158928, https://doi.org/10.1016/j.cej.2024.158928.

[3] J. Mazarío, S. Ghosh, V. Varela-Izquierdo, L.M. Martínez-Prieto, B. Chaudret, Magnetic Nanoparticles and Radio Frequency Induction: from specific heating to Magnetically Induced Catalysis, ChemCatChem 17 (2025) e202400683, https://doi.org/10.1002/cctc.202400683.

[4] P. Piqueras, M.J. Ruiz, J.M. Herreros, A. Tsolakis, Influence of the cell geometry on the conversion efficiency of oxidation catalysts under real driving conditions, Energy Convers. Manag. 233 (2021) 113888, https://doi.org/10.1016/j.enconman.2021.113888.

[5] A.M. Alkadhem, E. Perez-Botella, S. Pietsch-Braune, H.O. Mohamed, C.A. Grande, S. Heinrich, P. Castaño, Engineering Catalysts at the Multiscale: past, present, and Future of Catalyst Manufacturing and Shaping Processes, ChemCatChem 18 (2026) e01109, https://doi.org/10.1002/cctc.202501109.

[6] O. Al-Ketan, M. Pelanconi, A. Ortona, R.k. Abu Al-Rub, Additive manufacturing of architected catalytic ceramic substrates based on triply periodic minimal surfaces, J. Am. Ceram. Soc. 102 (2019) 6176–6193, https://doi.org/10.1111/jace.16474.

[7] I. Özden, A. Iveković, A. Kocjan, Additive manufacturing of ceramics from thermoplastic feedstocks, Open Ceram. 6 (2021) 100129, https://doi.org/10.1016/j.oceram.2021.100129.
[8] E. Schwarzer, M. Götz, D. Markova, D. Stafford, U. Scheithauer, T. Moritz, Lithography-based ceramic manufacturing (LCM) – Viscosity and cleaning as two quality influencing steps in the process chain of printing green parts, J. Eur. Ceram. Soc. 37 (2017) 5329–5338, https://doi.org/10.1016/j.jeurceramsoc.2017.05.046.
[9] V. Tomeckova, J.W. Halloran, Cure depth for photopolymerization of ceramic suspensions, J. Eur. Ceram. Soc. 30 (2010) 3023–3033, https://doi.org/10.1016/j.jeurceramsoc.2010.06.004.
[10] J. Essmeister, A.A. Altun, M. Staudacher, T. Lube, M. Schwentenwein, T. Konegger, Stereolithography-based additive manufacturing of polymer-derived SiOC/SiC ceramic composites, J. Eur. Ceram. Soc. 42 (2022) 5343–5354, https://doi.org/10.1016/j.jeurceramsoc.2022.06.021.
[11] P. Colombo, J.R. Hellmann, Ceramic foams from preceramic polymers, Mater. Res. Innov. 6 (2002) 260–272, https://doi.org/10.1007/s10019-002-0209-z.
[12] J. Essmeister, L. Schachtner, E. Szoldatits, S. Schwarz, A. Lichtenegger, B. Baumann, K. Föttinger, T. Konegger, Polymer-derived Ni/SiOC materials structured by vat-based photopolymerization with catalytic activity in CO2 methanation, Open Ceram. 14 (2023) 100350, https://doi.org/10.1016/j.oceram.2023.100350.
[13] E. Ionescu, C. Terzioglu, C. Linck, J. Kaspar, A. Navrotsky, R. Riedel, Thermodynamic Control of phase Composition and Crystallization of Metal-Modified Silicon Oxycarbides, J. Am. Ceram. Soc. 96 (2013) 1899–1903, https://doi.org/10.1111/jace.12327.
[14] C. Zhou, L. Yang, H. Geng, Q. Zheng, H. Min, Z. Yu, H. Xia, Preparation of Si–C–N–Fe magnetic ceramic derived from iron-modified polysilazane, Ceram. Int. 38 (2012) 6815–6822, https://doi.org/10.1016/j.ceramint.2012.05.080.
[15] Z. Yu, L. Yang, H. Min, P. Zhang, C. Zhou, R. Riedel, Single-source-precursor synthesis of high temperature stable SiC/C/Fe nanocomposites from a processable hyperbranched polyferrocenylcarbosilane with high ceramic yield, J. Mater. Chem. C 2 (2014) 1057–1067, https://doi.org/10.1039/C3TC32088J.
[16] M.M. Salehi, M. Mohammadi, A.R. Akbarzadeh, M. Babamoradi, A. Maleki, E. N. Zare, Advancements in preceramic inorganic polymers for environmental applications: properties, synthesis, and potential uses, RSC Adv. 15 (2025) 25514–25541, https://doi.org/10.1039/D5RA02047F.
[17] X. Lin, Z. Long, L. Jiang, Z. Liu, C. Liu, Z. Chen, 3D printed crack-free SiOC(Fe) structures with pyrolysis-induced carbon nanowires for enhanced wave absorption performance, Ceram. Int. 49 (2023) 33205–33213, https://doi.org/10.1016/j.ceramint.2023.08.028.
[18] Y. Feng, X. Guo, K. Huang, H. Elsayed, G. Franchin, H. Gong, P. Colombo, Enhanced electromagnetic microwave absorption of SiOC ceramics targeting the integration of structure and function, J. Eur. Ceram. Soc. 41 (2021) 6393–6405, https://doi.org/10.1016/j.jeurceramsoc.2021.06.007.
[19] J. Essmeister, A.-M. Fuchsberger, D. Steiner, S. Schwarz, T. Schachinger, A. Lale, M. Schwentenwein, K. Föttinger, T. Konegger, Hierarchically Porous Ceramic and Metal-Ceramic Hybrid Materials Structured by Vat Photopolymerization-Induced phase Separation, Adv. Mater. Technol. 9 (2024) 2301400, https://doi.org/10.1002/admt.202301400.
[20] A. Kumari, K. Singh, O. Hinrichsen, V.V. Buwa, Effect of catalytic structures on fluid flow and heat transfer characteristics using structure-resolved CFD simulations, Chem. Eng. J. 510 (2025) 161695, https://doi.org/10.1016/j.cej.2025.161695.
[21] S.H. Mian, C.K. Nirala, R. Kant, U. Umer, Computational evaluation based case study of Schwarz-P TPMS lattice architectures for heat sink thermal performance, Case Stud. Therm. Eng. 72 (2025) 106273, https://doi.org/10.1016/j.csite.2025.106273.
[22] E. Ionescu, C. Linck, C. Fasel, M. Müller, H. Kleebe, R. Riedel, Polymer-Derived SiOC/ZrO2 Ceramic Nanocomposites with Excellent High-Temperature Stability, J. Am. Ceram. Soc. 93 (2010) 241–250, https://doi.org/10.1111/j.1551-2916.2009.03395.x.
[23] F. Sarraf, A. Hadian, F. Gfeller, S.V. Churakov, F. Clemens, Crosslinking and pyrolysis of a methyl-silsesquioxane: effect of heating rate on fabrication of polymer derived mullite ceramics using thermoplastic shaping, Mater. Des. 237 (2024) 112578, https://doi.org/10.1016/j.matdes.2023.112578.
[24] R.A. Meyers, INTERPRETATION OF INFRARED SPECTRA , a PRACTICAL APPROACH 1 Interpretation of Infrared Spectr, A Practical Approach, in (2000).
[25] C. Zhou, S. Li, Z. Yu, Polymer-derived FeSi/SiC@SiOC ceramic nanocomposites with tunable microwave absorption behavior, Int. J. Appl. Ceram. Technol. 19 (2022) 813–827, https://doi.org/10.1111/ijac.13850.
[26] M. Hojamberdiev, R.M. Prasad, C. Fasel, R. Riedel, E. Ionescu, Single-source-precursor synthesis of soft magnetic Fe3Si- and Fe5Si3-containing SiOC ceramic nanocomposites, J. Eur. Ceram. Soc. 33 (2013) 2465–2472, https://doi.org/10.1016/j.jeurceramsoc.2013.04.005.
[27] L. Chen, J. Zhao, L. Wang, F. Peng, H. Liu, J. Zhang, J. Gu, Z. Guo, In-situ pyrolyzed polymethylsilsesquioxane multi-walled carbon nanotubes derived ceramic nanocomposites for electromagnetic wave absorption, Ceram. Int. 45 (2019) 11756–11764, https://doi.org/10.1016/j.ceramint.2019.03.052.
[28] D. Schmitt, O. Janka, R. Leiner, G. Kickelbick, M. Gallei, Preparation of preceramic ferrocene-modified microparticles for the development of uniform porous iron oxide particles and their sustainable recycling, Mater. Adv. 5 (2024) 3037–3050, https://doi.org/10.1039/D3MA01131C.
[29] E. Ionescu, B. Papendorf, H.-J. Kleebe, F. Poli, K. Müller, R. Riedel, Polymer-Derived Silicon Oxycarbide/Hafnia Ceramic Nanocomposites. Part I: phase and Microstructure Evolution during the Ceramization Process, J. Am. Ceram. Soc. 93 (2010) 1774–1782, https://doi.org/10.1111/j.1551-2916.2010.03765.x.
[30] G. Mitteramskogler, R. Gmeiner, R. Felzmann, S. Gruber, C. Hofstetter, J. Stampfl, J. Ebert, W. Wachter, J. Laubersheimer, Light curing strategies for lithography-based additive manufacturing of customized ceramics, Addit. Manuf. 1–4 (2014) 110–118, https://doi.org/10.1016/j.addma.2014.08.003.
[31] C.R. Woof, D.J. Durand, N. Fey, E. Richards, R.L. Webster, Iron Catalyzed double Bond Isomerization: evidence for an FeI/FeIII Catalytic Cycle, Chem. – A Eur. J. 27 (2021) 5972–5977, https://doi.org/10.1002/chem.202004980.
[32] F. Sarraf, S.V. Churakov, F. Clemens, Preceramic Polymers for Additive Manufacturing of Silicate Ceramics, Polymers (basel). 15 (2023), https://doi.org/10.3390/polym15224360.
[33] B. Hong, C. Qianwang, S. Tao, Preparation of ferromagnetic γ - Fe2O3 nanocrystallites by oxidative co-decomposition of PEG 6000 and ferrocene, Solid State Commun. 141 (2007) 573–576, https://doi.org/10.1016/j.ssc.2006.12.011.
[34] S. Grimm, P. Hemberger, T. Kasper, B. Atakan, Mechanism and Kinetics of the thermal Decomposition of Fe(C5H5)2 in Inert and Reductive Atmosphere: a Synchrotron-Assisted Investigation in a Microreactor, Adv. Mater. Interfaces 9 (2022) 2200192, https://doi.org/10.1002/admi.202200192.
[35] M. Thommes, K. Kaneko, A.V. Neimark, J.P. Olivier, F. Rodriguez-Reinoso, J. Rouquerol, K.S.W. Sing, Physisorption of gases, with special reference to the evaluation of surface area and pore size distribution (IUPAC, Technical Report) 87 (2015) 1051–1069, https://doi.org/10.1515/pac-2014-1117.
[36] J. Wang, H. Zhang, X. Liu, K. Xia, The Fe-Incorporation Effects on the Structural Evolution of SiOC Ceramics, SILICON 16 (2024) 4787–4796, https://doi.org/10.1007/s12633-024-03046-0.
[37] P. Xu, X.J. Han, X.R. Liu, B. Zhang, C. Wang, X.H. Wang, A study of the magnetic and electromagnetic properties of γ-Fe2O3–multiwalled carbon nanotubes (MWCNT) and Fe/Fe3C–MWCNT composites, Mater. Chem. Phys. 114 (2009) 556–560, https://doi.org/10.1016/j.matchemphys.2008.10.010.
[38] Z. Chen, X. Li, J. Wang, W. Li, Preparation of continuous Si-Fe-C-O functional ceramic fibers, Trans. Nonferrous Met. Soc. China 17 (2007) 987–991, https://doi.org/10.1016/S1003-6326(07)60212-X.
[39] A. Bhattacharjee, A. Rooj, D. Roy, M. Roy, Thermal Decomposition Study of Ferrocene [(C5H5)2Fe], J. Exp. Phys. 2014 (2014) 513268, https://doi.org/10.1155/2014/513268.
[40] B. Du, A. Wang, T. Zhang, D. Liu, Phase development in metal-dropped silicon oxycarbides under water vapor and argon hybrid atmosphere, Ceram. Int. 48 (2022) 19720–19731, https://doi.org/10.1016/j.ceramint.2022.03.235.
[41] R.J. Longbottom, O. Ostrovski, J. Zhang, D. Young, Stability of Cementite formed from Hematite and Titanomagnetite Ore, Metall. Mater. Trans. B 38 (2007) 175–184, https://doi.org/10.1007/s11663-006-9005-2.
[42] J.M.D. Coey, Magnetism and magnetic materials, Cambridge university press, 2010.
[43] C. Appino, O. de la Barrière, F. Fiorillo, M. LoBue, F. Mazaleyrat, C. Ragusa, Classical eddy current losses in soft magnetic composites, J. Appl. Phys. 113 (2013) 17A322, https://doi.org/10.1063/1.4795744.
[44] J. Carrey, B. Mehdaoui, M. Respaud, Simple models for dynamic hysteresis loop calculations of magnetic single-domain nanoparticles: Application to magnetic hyperthermia optimization, J. Appl. Phys. 109 (2011) 83921, https://doi.org/10.1063/1.3551582.
[45] C. Díaz-Ufano, A. Gallo-Cordova, L. Santiandreu, S. Veintemillas-Verdaguer, R. Sáez, M.J. Torralvo Fernández, M. del, P. Morales, Maximizing the adsorption capacity of iron oxide nanocatalysts for the degradation of organic dyes, Colloids Surfaces A Physicochem. Eng. Asp. 658 (2023) 130695, https://doi.org/10.1016/j.colsurfa.2022.130695.
[46] J.M. Asensio, A.B. Miguel, P.-F. Fazzini, P.W.N.M. van Leeuwen, B. Chaudret, Hydrodeoxygenation using magnetic Induction: High-Temperature Heterogeneous Catalysis in solution, Angew. Chem. Int. Ed. Engl. 58 (2019) 11306–11310, https://doi.org/10.1002/anie.201904366.
[47] S.-H. Lin, W. Hetaba, B. Chaudret, W. Leitner, A. Bordet, Copper-decorated Iron Carbide Nanoparticles Heated by magnetic Induction as Adaptive Multifunctional Catalysts for the Selective Hydrodeoxygenation of Aldehydes, Adv. Energy Mater. 12 (2022) 2201783, https://doi.org/10.1002/aenm.202201783.
[48] A. Bordet, W. Leitner, Adaptive Catalytic Systems for Chemical Energy Conversion, Angew. Chemie Int. Ed. 62 (2023) e202301956, https://doi.org/10.1002/anie.202301956.
[49] L. Truong-Phuoc, C. Duong-Viet, J.-M. Nhut, A. Pappa, S. Zafeiratos, C. Pham-Huu, Induction heating for the Electrification of Catalytic Processes, ChemSusChem 18 (2025) e202402335, https://doi.org/10.1002/cssc.202402335.